Chinese Chemical Letters 36 (2025) 110168

Contents lists available at ScienceDirect

Chinese Chemical Letters

journal homepage: www.elsevier.com/locate/cclet

Ru(II)-based aggregation-induced emission (AIE) agents with efficient $^1O_2$ generation, photo-catalytic NADH oxidation and anticancer activity

Yunli Xu[a,b], Xuwen Da[a], Lei Wang[c], Yatong Peng[a,b], Wanpeng Zhou[a,b], Xiulian Liu[a,b], Yao Wu[a,b], Wentao Wang[c], Xuesong Wang[a,b,*], Qianxiong Zhou[a,*]

[a] Key Laboratory of Photochemical Conversion and Optoelectronic Materials, Technical Institute of Physics and Chemistry, Chinese Academy of Sciences, Beijing 100190, China
[b] University of Chinese Academy of Sciences, Beijing 100049, China
[c] Wenzhou Institute, University of Chinese Academy of Sciences, Wenzhou 325000, China

ARTICLE INFO

Article history:
Received 22 April 2024
Revised 20 June 2024
Accepted 21 June 2024
Available online 22 June 2024

Keywords:
Ru(II) complexes
Aggregation-induced emission
Photo-catalytic NADH oxidation
Photodynamic therapy
Turnover frequency

ABSTRACT

Photodynamic therapy (PDT) has received much attention in recent years. However, traditional photosensitizers (PSs) applied in PDT usually suffer from aggregation-caused quenching (ACQ) effect in H_2O, single and inefficient photochemical mechanism of action (MoA), poor cancer targeting ability, *etc*. In this work, two novel Ru(II)-based aggregation-induced emission (AIE) agents (Ru1 and Ru2) were developed. Both complexes exhibited long triplet excited lifetimes and nearly 100% singlet oxygen quantum yields in H_2O. In addition, Ru1 and Ru2 displayed potent photo-catalytic reduced nicotinamide adenine dinucleotide (NADH) oxidation activity with turnover frequency (TOF) values of about 1779 and 2000 h^{-1}, respectively. Therefore, both Ru1 and Ru2 showed efficient PDT activity towards a series of cancer cells. Moreover, Ru2 was further loaded in bovine serum albumin (BSA) to enhance the tumor targeting ability *in vivo*, and the obtained Ru2@BSA could selectively accumulate in tumor tissues and effectively inhibit tumor growth on a 4T1 tumor-bearing mouse model. So far as we know, this work represents the first report about Ru(II) AIE agents that possess high singlet oxygen quantum yields and also potent photo-catalytic NADH oxidation activity, and may provide new ideas for rational design of novel PSs with efficient PDT activity.

Cancer has long been a global health problem [1]. The suboptimal efficacy and undesired side-effects of conventional cancer treatments (such as surgery, radiotherapy, chemotherapy) highlights the urgency to develop alternative strategies [2–4]. Photodynamic therapy (PDT) which relies on the combination of photosensitizers (PSs), oxygen, and light to generate reactive oxygen species (ROS) to kill cancer cells, has received much attention in the past decades due to its unique advantages, including non-invasiveness, precise spatiotemporal control, and low systemic toxicity [5–7]. Upon irradiation, the excited PSs can generally produce singlet oxygen ($^1O_2$) through energy transfer with surrounding molecular oxygen (type-II mechanism), or participate in a cascade of electron transfer processes to create radical intermediates, such as superoxide anion radicals ($O_2^{\bullet-}$), hydroxyl radicals ($^{\bullet}OH$), and peroxides (O_2^{2-}) (type-I mechanism). PSs play a crucial role in PDT, and most PSs for clinical application are tetrapyrrolic derivatives, including porphyrins, phthalocyanines and chlorins [8–11]. Despite their widespread use, these compounds still have some inherent drawbacks such as low water solubility, aggregation-caused quenching (ACQ) effect, single and inefficient photochemical mechanism of action (MoA), poor cancer-targeting ability, *etc*. Therefore, novel PSs that can address these issues are highly desirable.

In addition to organic PSs, transition metal complexes, especially Ru(II) compounds have also garnered significant attention for PDT due to their desirable photophysical, photochemical and electrochemical properties [12–14]. Noteworthy, a Ru(II)-based PS, namely TLD1433, has been in phase II clinical trials against non-muscle invasive bladder cancer [15], fully demonstrating the potential of Ru(II)-based PSs for PDT application. Generally, Ru(II)-based PSs have long-lived and efficiently populated triplet metal-to-ligand charge transfer (^{3}MLCT) states by virtue of the heavy atom effect, which is favorable for ROS production through the classic type-I/II mechanisms. Besides, recently the photoredox catalysis capability of metal complexes was also explored for oxidizing intracellular important biomolecules, such

* Corresponding authors.
E-mail addresses: xswang@mail.ipc.ac.cn (X. Wang), zhouqianxiong@mail.ipc.ac.cn (Q. Zhou).

https://doi.org/10.1016/j.cclet.2024.110168
1001-8417/

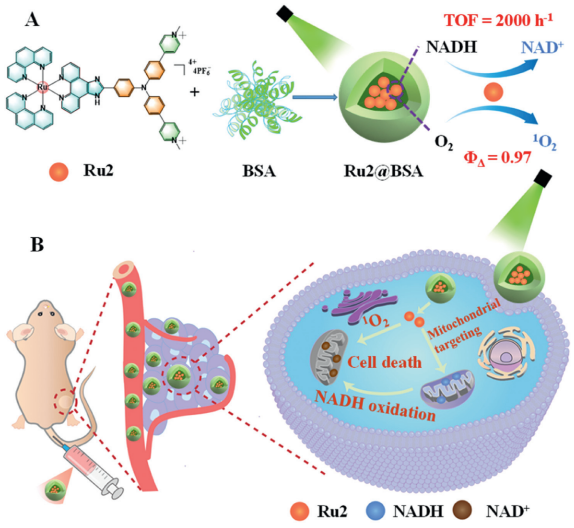

Scheme 1. (A) Schematic illustration of fabrication and properties of Ru2@BSA, and (B) its application for PDT *in vivo*.

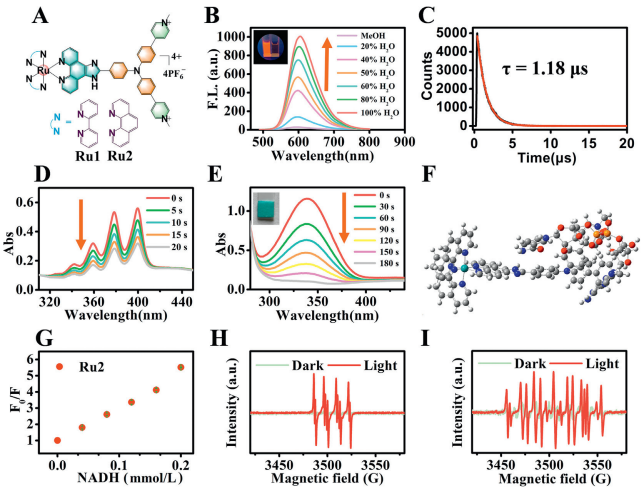

Fig. 1. (A) Chemical structures of Ru1 and Ru2. (B) Emission spectra of Ru2 in mixed CH_3OH/H_2O solvents with different water fractions. (C) Emission decay of Ru2 in H_2O under an argon atmosphere. (D) $^1O_2$ generation of Ru2 in H_2O upon 470 nm light irradiation (22.5 mW/cm^2), using 9,10-ADPA (50 μmol/L) as a chemical trap. (E) Photo-catalytic oxidation of NADH (200 μmol/L) by Ru2 (2 μmol/L) in water upon 470 nm light irradiation. Inset is the result of H_2O_2 test paper. (F) Optimized conformation between Ru2 and NADH based on DFT calculations. (G) Stern–Volmer luminescence quenching plot of Ru2 by NADH. F_0 and F are the emission intensities in the absence and presence of NADH, respectively. (H) ESR spectra of the mixed solutions containing Ru2 (10 μmol/L) and NADH (200 μmol/L) using DMPO (20 mmol/L) as the $O_2^{\bullet-}$ trapping agent with or without light irradiation (470 nm, 22.5 mW/cm^2). (I) ESR spectra of NAD$^\bullet$ radical obtained upon irradiation (470 nm, 22.5 mW/cm^2) of Ru2 (2 mmol/L) in methanol/PBS (1:1) solution in the presence of NADH (20 mmol/L) and CYPMPO (2 mmol/L).

as reduced nicotinamide adenine dinucleotide (NADH) [16,17]. NADH plays pivotal roles in maintaining intracellular redox balance, energy production, biomolecules synthesis, *etc.* [18,19]. Consequently, perturbations in the NADH/oxidized nicotinamide adenine dinucleotide (NAD^+) balance caused by photoredox catalysis have the potential to induce cell death, thus contributing to a photo-catalytic antitumor mechanism of action that differs from classic type I/II processes [20–22]. Our work demonstrated Ru(II)-based PSs were good candidates for photo-catalytic NADH oxidation [23–27]. For example, a turnover frequency (TOF) value of about 700 h^{-1} was obtained for $[Ru(phen)_2(PIP–OCH_3)](PF_6)_2$ (phen = 1,10-phenanthroline, PIP–OCH_3 = 2-(4-methoxyphenyl)-1*H*-imidazo[4,5-*f*][1,10]phenanthroline) and a Ru(II)-nitro-anthraquinone supramolecule upon 470 nm light irradiation (22.5 mW/cm^2) [24,27]. After examining a series of well-known organic PSs, such as boron dipyrromethene (BODIPY), phenoselenazinium, Rose Bengal, phthalocyanine, porphyrin and derivatives, Sessler, Peng, Kim and co-authors have disclosed that such photoredox catalysis may be a general mechanism in PDT [28]. Nevertheless, PSs with highly efficient photo-catalytic NADH oxidation activity are still rare.

Aggregation-induced emission (AIE) which was coined by Tang's group in 2001 [29], has received much attention in the past decades. AIE based PSs exhibit weak or no emission in the dilute solutions, but switch to highly emissive in the aggregated or solid state. AIE holds significant promise in overcoming the notorious ACQ effect observed in common PSs, which is favorable to increase PDT efficacy [30–33]. A lot of organic AIE agents have been developed for PDT application in the last ten years, while metal complexes based AIE PSs are relatively rare [34–36]. The presence of metal atoms will facilitate intersystem crossing (ISC), which can enhance the population efficiency of long-lived triplet excited states and consequent ROS generation. Moreover, through carefully tailoring the chemical structures of AIE groups to strengthen the binding affinity between PSs and NADH, the photo-catalytic NADH oxidation activity may be simultaneously improved. Based on these considerations, herein we have successfully designed and synthesized two novel Ru(II) AIE agents (Ru1 and Ru2, Scheme 1 and Fig. 1A), in which a triphenylamine (TPA) group functionalized with pyridine cations was integrated onto the PIP (PIP = 2-phenylimidazo[4,5-*f*][1,10]phenanthroline) ligand. Ru1 and Ru2 possess long triplet ^{3}MLCT lifetimes (about 1 μs) and nearly 100% singlet oxygen quantum yields in aqueous solutions. Moreover, upon 470 nm light irradiation (22.5 mW/cm^2), both Ru1 and Ru2 exhibited potent photo-catalytic NADH oxidation activity, achieving high TOF values of about 1779 and 2000 h^{-1}, respectively. This enhanced performance is likely attributed to the strengthened affinity between Ru1/Ru2 and NADH. To enhance the tumor targeting ability, Ru2 was further encapsulated in bovine serum albumin (BSA) with high binding affinity towards glycoprotein 60 (gp60) overexpressed on the membranes of many cancer cells [23,37–40], and the resultant Ru2@BSA exhibited targeted and efficient PDT activity both *in vitro* and *in vivo*.

The synthetic routes for Ru1 and Ru2 were shown in Scheme S1 (Supporting information). The TPA group was introduced as the typical AIE responsive unit, and pyridine cations were further modified on TPA to enhance the binding affinity with anionic NADH through electrostatic interaction. Both complexes were fully characterized by ^{1}H nuclear magnetic resonance (NMR), ^{13}C NMR, electrospray ionization mass spectrometry (ESI-MS) and high performance liquid chromatography (HPLC) (Figs. S1–S7 in Supporting information).

As displayed in Fig. S8 (Supporting information), Ru1 and Ru2 show typical ^{1}MLCT absorption in the visible region in H_2O, with peaks at 427 and 428 nm, respectively. The emission peaks of Ru1 and Ru2 in H_2O are separately situated at 609 nm and 604 nm. Typical AIE behavior was observed for both Ru1 and Ru2 (Fig. 1B and Fig. S9 in Supporting information). In the good solvent CH_3OH, the emission intensity of these compounds is relatively weak. However, as the proportions of the poor solvent H_2O increase, the emission intensity gradually intensifies, exhibiting the characteristic AIE effect. The emission lifetimes in H_2O were measured to be 1.03 and 1.18 μs for Ru1 and Ru2 (Fig. 1C and Fig. S10 in Supporting information), respectively, which are much longer than that (0.55 μs) of the prototype compound $[Ru(bpy)_3]^{2+}$ (Ru0, bpy = 2,2′-bipyridine). The emission lifetime values of Ru1 and Ru2 align closely with the excited lifetimes obtained by nanosec-

ond transient absorption spectroscopy (Fig. S10), confirming their ^{3}MLCT emission nature.

The long ^{3}MLCT lifetimes of Ru1 and Ru2 in H_2O are favorable for $^1O_2$ generation through energy transfer, therefore their $^1O_2$ quantum yields were firstly measured using 3,3′-(anthracene-9,10-diyl) dipropanoic acid (9,10-ADPA) as the chemical trapping agent and Ru0 as the reference ($\Phi = 0.41$ in H_2O) [41]. As shown in Fig. 1D and Fig. S11 (Supporting information), Ru1 and Ru2 could quickly bleach the absorption of 9,10-ADPA upon 470 nm light irradiation, indicative of efficient $^1O_2$ generation ability. The $^1O_2$ quantum yields were determined as 0.90 and 0.97 for Ru1 and Ru2, respectively, much higher than that of Ru0. In sharp contrast, in the good solvent acetonitrile, the $^1O_2$ quantum yields of Ru1 ($\Phi = 0.38$) and Ru2 ($\Phi = 0.40$) are much lower, which indicates that the AIE character of Ru1 and Ru2 is essential for $^1O_2$ generation in aqueous solutions (Fig. S12 in Supporting information). This is totally different from that of common PSs such as porphyrin, phthalocyanine, which usually have low ROS generation in H_2O due to the ACQ effect. Besides, electron spin resonance (ESR) spectroscopy with 2,2,6,6-tetramethyl-4-piperidone (TEMP) as the spin-trapping agent was further utilized to identify $^1O_2$ production. As shown in Fig. S13 (Supporting information), a three-line signal with equal intensity was detected for the mixture of Ru1/Ru2 and TEMP upon light-irradiation, which can be ascribed to TEMPO (the adduct of TEMP and $^1O_2$).

Ru(II) complexes have been reported as effective photo-catalysts for NADH oxidation [16,17,23,24,27,42,43]. Therefore, the performances of Ru1 and Ru2 were thoroughly examined. NADH has a characteristic absorption peak at ~338 nm and an emission peak at ~450 nm, which will disappear after oxidation into NAD^+ [26]. As shown in Fig. 1E, Figs. S14 and S15 (Supporting information), the absorbance and emission of NADH (200 μmol/L) quickly decreased in the presence of Ru1/Ru2 (2 μmol/L) and light irradiation (470 nm, 22.5 mW/cm^2), indicating efficient photo-catalytic NADH oxidation. Accompanied by NADH oxidation, H_2O_2 production was detected using H_2O_2 test paper (insets of Fig. 1E and Fig. S14A), consistent with previous reports. Control experiments showed that Ru1/Ru2 and light are both necessary (Fig. S16 in Supporting information), aligning with the photo-catalytic mechanism. After irradiation for 180 s, the TOF values for Ru1 and Ru2 were calculated to be 1779 and 2000 h^{-1}, respectively, which are much higher than that of Ru0 (225 h^{-1}, Fig. S17 in Supporting information) and other reported Ru(II) complexes (about 700 h^{-1}) under 470 nm irradiation with the same light intensity [24,27]. In the context of photo-catalytic NADH oxidation, the single electron transfer (SET) between NADH and the excited PSs has been identified as the rate-limiting step [44]. The relatively long ^{3}MLCT lifetimes of Ru1 and Ru2 are favorable for photo-induced intermolecular electron transfer. The efficiency of Ru2 photo-catalytic oxidation of NADH is slightly superior to that of Ru1, primarily due to the marginally longer triplet lifetime exhibited by Ru2 compared to Ru1. In addition, the AIE group in Ru1 and Ru2 may enhance the binding affinity with NADH *via* π-π stacking and electrostatic interactions, therefore improving the photo-catalytic activity. Taking Ru2 as an example, density functional theory (DFT) calculations demonstrate formation of a relatively stable "clamped" complex between NADH and Ru2 (Fig. 1F). Besides, upon titration with NADH, the NMR peak of Ru2, with a chemical shift at 7.42 ppm, which can be ascribed to protons based on the triphenylamine moiety, gradually shifted to 7.25 ppm (Fig. S18 in Supporting information), indicating the occurrence of a static interaction [24,43]. Under the same conditions, no obvious changes were observed for the NMR spectra of Ru0 (Fig. S19 in Supporting information), indicating the important role of the AIE groups in Ru1/Ru2.

The photo-catalytic NADH oxidation was further examined by ^{1}H NMR spectra, taking Ru2 as an example. As shown in Fig. S20 (Supporting information), NAD^+ based new peaks at 8.85, 9.21, and 9.38 ppm, appeared for the mixed solution of Ru2 and NADH after irradiation, confirming that Ru2 can photo-catalytically oxidize NADH into NAD^+. A Stern-Volmer titration was conducted to gain insights into the mechanism of photo-catalytic NADH oxidation. As the concentration of NADH was increased, a gradual decrease in the luminescence intensity of Ru1 and Ru2 (2 μmol/L) was observed (Figs. S21A and B in Supporting information), suggesting a reduction quenching process. In the presence of 200 μmol/L NADH, the emission of Ru1 and Ru2 were significantly quenched by 56% and 82%, respectively. The fitted quenching rate constants (K) were determined to be 1.05×10^4 L/mol for Ru1 and 2.16×10^4 L/mol for Ru2 (Fig. 1G and Fig. S21C in Supporting information). Under identical conditions, the luminescence intensity of Ru0 only exhibited a slight decrease, yielding a K value of 3.39×10^2 L/mol (Fig. S22 in Supporting information). A larger K value means a more efficient electron transfer from NADH to the PS. Among these complexes, Ru2 possesses the largest K value, which is in line with its most efficient photo-catalytic NADH oxidation activity.

According to the previous reports [20], $O_2^{\bullet-}$ and $NAD^\bullet$ radicals were formed in the process of photo-catalytic NADH oxidation. To verify this, ESR spectroscopy was further used to detect these radical intermediates. The generation of $O_2^{\bullet-}$ was captured by using 5,5-dimethyl-1-pyrroline *N*-oxide (DMPO) as a spin trapping agent. As depicted in Fig. 1H, a photo-induced strong signal of DMPO–$O_2^{\bullet-}$ adduct was observed for the mixed solution containing Ru2 and NADH, indicating effective photo-induced electron transfer from NADH to Ru2, followed by further electron transfer to O_2 to produce $O_2^{\bullet-}$. In addition, 5-(2,2-dimethyl-1,3-propoxycyclophosphoryl)-5-methyl-1-pyrroline-*N*-oxide (CYPMPO) was used as a trapping agent for $NAD^\bullet$. Upon light irradiation, a carbon-centered $NAD^\bullet$ radical was detected (Fig. 1I). Similar results were obtained for Ru1 (Fig. S23 in Supporting information). Based on the results above, a possible mechanism for photo-catalytic NADH oxidation was depicted in Fig. S24 (Supporting information).

The ROS production and NADH depletion activities of Ru1 and Ru2 were further investigated within cells. 2′,7′-Dichlorodihydrofluorescein diacetate (DCFH-DA) was used as a ROS probe to visualize intracellular ROS levels by confocal laser scanning microscopy (CLSM). DCFH-DA is non-emissive but can be transformed into 2′,7′-dichlorofluorescein (DCF) with strong green fluorescence by intracellular ROS. HeLa (human cervix cancer) cells treated with light-irradiated phosphate buffer solution (PBS). and Ru1/Ru2 in the dark exhibited negligible green fluorescence (Fig. 2A and Fig. S25 in Supporting information). However, strong green fluorescence was observed for cells treated with Ru1/Ru2 and light irradiation, indicating their efficient photo-induced ROS generation within cells. Next, we delved into photo-induced intracellular NADH depletion using commercial NADH detection kits. The NADH levels within A549 (human lung cancer) cells remained unaltered upon treatment with Ru2 in darkness (Fig. 2B). However, upon light irradiation (470 nm, 22.5 mW/cm^2) for 30 min, a profound decrease in NADH levels could be observed. Specifically, 2 μmol/L of Ru2 upon light irradiation could lead to an 80% reduction of intracellular NADH content.

The efficient intracellular ROS generation and NADH depletion can cause cancer cell death. Therefore, the cytotoxicity of Ru1 and Ru2 against a series of cancer cell lines, including A549 cells, A549/DDP (cisplatin-resistant A549) cells, and HeLa cells were assessed employing the MTT assay. Ru1 and Ru2 demonstrated minimal dark cytotoxicity, with half maximal inhibitory concentration (IC_{50}) values exceeding 120 μmol/L (Table S1 and Figs. S26–S28 in Supporting information). However, upon exposure to light irradiation (470 nm, 22.5 mW/cm^2) for 30 min, a significant reduction in cancer cell viability was observed for both Ru1 and Ru2 (Fig. 2C). Specifically, Ru1 demonstrated IC_{50} values of approx-

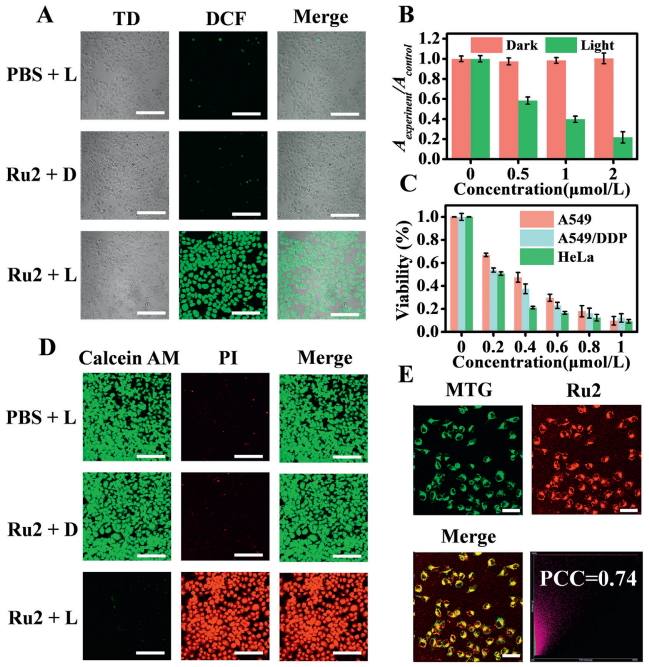

Fig. 2. (A) CLSM images of ROS levels in HeLa cells using DCFH-DA as the probe. Scale bar: 200 μm. (B) NADH levels of A549 cells treated with varied concentrations of Ru2 with or without irradiation. (C) Photo-cytotoxicity of Ru2 against a series of cancer cell lines. (D) CLSM images of HeLa cells upon different treatments and stained with calcein-AM/PI. Scale bar: 200 μm. (E) CLSM images of HeLa cells co-stained by Ru2 and MTG. Scale bar: 50 μm. "D" and "L" denote "dark" and "light", respectively. Data are presented as mean ± standard deviation (SD) ($n = 3$).

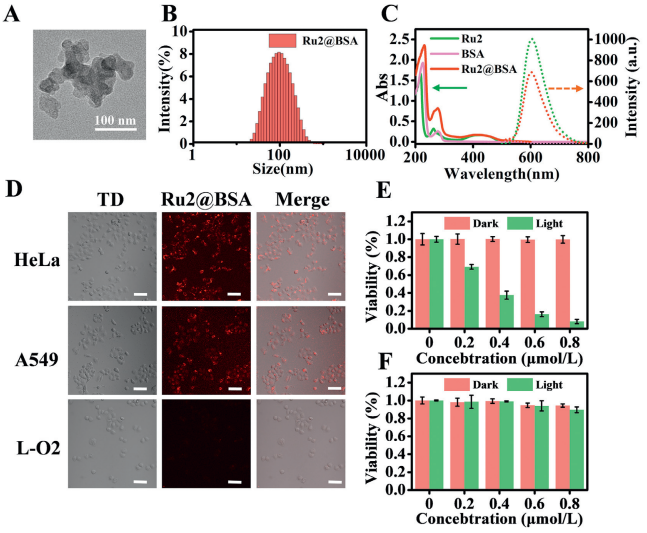

Fig. 3. (A) TEM image of Ru2@BSA. (B) Particle size distribution of Ru2@BSA measured by DLS. (C) Absorption (solid line) and emission (dashed line) spectra of Ru2, BSA and Ru2@BSA. (D) CLSM images of HeLa, A549 and L-O2 cells after incubation with Ru2@BSA. Scale bar: 100 μm. (E) Cytotoxicity of Ru2@BSA towards HeLa and (F) L-O2 cells in the dark or upon 470 nm light irradiation for 30 min (22.5 mW/cm^2). Data are presented as mean ± SD ($n = 3$).

imately 0.4 μmol/L against HeLa cells and 0.6 μmol/L against A549 cells, whereas Ru2 exhibited IC_{50} values of about 0.2 and 0.4 μmol/L against these two cell lines, respectively. Compared with Ru1, the higher singlet oxygen quantum yield and photocatalytic NADH oxidation activity of Ru2 should mainly account for its slightly increased photo-cytotoxicity. Remarkably, Ru1 and Ru2 also exhibited similar photo-cytotoxicity against cisplatin-resistant A549/DDP cells, yielding IC_{50} values of about 0.4 and 0.2 μmol/L, respectively. However, the typical chemotherapeutic anticancer agent, cisplatin, displayed much lower anticancer activity, especially towards A549/DDP cells with an IC_{50} value exceeding 100 μmol/L (Table S1 and Fig. S29 in Supporting information).

To further visualize the anticancer activity, calcein-AM/propidium iodide (PI) co-staining assays were employed [45]. Live cells can be stained by calcein-AM with green fluorescence, while apoptotic cells will be stained by PI with red fluorescence. As shown in Fig. 2D, HeLa cells treated with PBS + L or Ru2 + D exhibited strong green emission of calcein-AM, indicating most of the cells were alive. In contrast, almost only red fluorescence of PI was observed for cells treated with Ru2 and light irradiation, consistent with its high photo-cytotoxicity.

In addition to the photophysical and photochemical properties, the subcellular distribution of PSs also plays an important role in their anticancer activity. It has been reported that many Ru(II) complexes are prone to accumulate in mitochondria [25,46]. Mitochondria are rich in NADH, and have key roles in energy production and apoptosis [20,47], thus are ideal intracellular targets for drug design. Taking Ru2 as an example, its subcellular localization was further investigated by co-staining with mitochondria specific fluorescent probe Mito-Tracker Green (MTG). The co-localization CLSM imaging results revealed a remarkable overlap between the red luminescence of Ru2 and green emission of MTG ($P = 0.74$), indicating that it is mainly distributed in mitochondria (Fig. 2E). Considering the efficient photo-catalytic NADH oxidation and $^1O_2$ generation, it is anticipated that Ru2 can cause effective damage to mitochondria. Mitochondria damage can be monitored by detecting the changes of mitochondrial membrane potentials ($\Delta\Psi m$). 5,5′,6,6′-Tetrachloro-1,1′−3,3′-tetraethylbenzimidazolylcarbo-cyanineiodide (JC-1) [48,49], a mitochondria selective dye is often used to probe $\Delta\Psi m$. JC-1 emits red fluorescence in the form of "J-aggregates" when $\Delta\Psi m$ is high, but green fluorescence in the form of "J-monomer" when $\Delta\Psi m$ is compromised due to damage. As shown in Fig. S30 (Supporting information), almost only green fluorescence of "J-monomer" was observed for HeLa cells treated with Ru2 and irradiation, indicating severe mitochondria damage.

To enhance the tumor targeting ability *in vivo*, Ru2 was further loaded in BSA to take full advantage of the high binding affinity of BSA towards gp60 receptors overexpressed on the membranes of many cancer cells. The obtained Ru2@BSA nanoparticles were characterized by transmission electron microscopy (TEM), dynamic light scattering (DLS), as well as absorption and emission spectra. As shown in Fig. 3A, the TEM image displays Ru2@BSA has a nearly spherical morphology with an average diameter of 60 ± 5 nm. Scanning transmission electron microscopy (STEM) and energy-dispersive X-ray spectroscopy (EDS) elemental mapping images demonstrate the presence of Ru-based signals along with that of N, O, and S elements (Fig. S31 in Supporting information), indicating successful encapsulation of Ru2 within the BSA matrix. Ru2@BSA can be well dispersed in water with a DLS diameter of ~100 nm (Fig. 3B), which is slightly larger than the TEM result probably due to the water layer outside the particles. The absorption and emission spectra of Ru2@BSA clearly show Ru2-based absorption and emission, confirming the successful loading of Ru2 (Fig. 3C).

Thanks to the emissive character of Ru2@BSA, its tumor targeting ability can be readily investigated by CLSM imaging. As shown in Fig. 3D, obvious red luminescence of Ru2 could be observed in HeLa and A549 cancer cells, while very faint signals appeared in normal L-O2 (hepatocyte cell) cells under the same conditions. The specific interaction of BSA with gp60 receptors overexpressed on the membranes of tumor cells will facilitate cell uptake. Such an active targeting ability in combination with the selec-

tive light irradiation will greatly minimize the possible side effects of Ru2@BSA.

The cytotoxicity of Ru2@BSA was evaluated against A549, HeLa, 4T1 (murine breast cancer cells) cancer cells, and L-O2 normal cells using the MTT assay. As shown in Fig. 3E and Fig. S32 (Supporting information), Ru2@BSA exhibited minimal dark-cytotoxicity against A549, HeLa, and 4T1 cancer cells, but remarkable photo-cytotoxicity with IC_{50} values of approximately 0.4–0.6 μmol/L upon 470 nm light irradiation (22.5 mW/cm^2) for 30 min. Notably, Ru2@BSA displayed significantly reduced photo-cytotoxicity towards normal L-O2 cells under the same conditions (Fig. 3F), which can be ascribed to the much lower uptake level as observed in Fig. 3D. Furthermore, the intracellular ROS generation of Ru2@BSA was also investigated using DCFH-DA as the probe. Upon irradiation, the strong green fluorescence of DCF was observed only in A549 and HeLa cancer cells but not in L-O2 normal cells (Fig. S33 in Supporting information), which is consistent with results above.

The cell death mechanism caused by Ru2@BSA was further investigated by the Annexin V-fluorescein isothiocyanate (FITC)/PI co-staining assay, the results of which were quantitatively analyzed by flow cytometry. As shown in Fig. S34 (Supporting information), compared with the control groups, the population in the top right quadrant (corresponding to late apoptotic cells) significantly increased for A549 cells treated with Ru2@BSA and light irradiation, indicating a late apoptosis mechanism.

Motivated by the efficient and targeted anticancer activity *in vitro*, the performances of Ru2@BSA *in vivo* were further assessed on a 4T1 tumor-bearing mouse model (Fig. 4A). All animal experiments were carried out with the permission of the Ethics Committee of Technical Institute of Physics and Chemistry, CAS (IACUC-IPC-22066). Firstly, to investigate the tumor targeting capability, Cy5.5-labeled Ru2@BSA was intravenous *via* the tail vein. As displayed in Fig. 4B, the fluorescence signal within the tumor region gradually intensified over time and reached its peak approximately 6 h post-injection. Two main factors should account for the effective tumor targeting of Ru2@BSA. Beyond the well-established enhanced permeability and retention (EPR) effects of nanoparticles [50], the active targeting capability of BSA also plays an important role for the selective accumulation within tumor tissues.

Finally, the anticancer activity of Ru2@BSA in 4T1 tumor-bearing mice was studied. When the tumors grew up to about 50 mm^3, all the mice were randomly divided into three groups with each group consisting of five mice: (I) PBS + L, (II) Ru2@BSA + D, and (III) Ru2@BSA + L (D and L denote dark and light, respectively). Ru2@BSA with a dosage of 50 mg/kg (about 0.5 mg/kg in Ru2) was injected *via* the tail vein. The light groups underwent exposure to a 520 nm laser (100 mW/cm^2 for 10 min) 6 h after intravenous injection. This treatment protocol was repeated continuously for three days. Throughout the 16-day treatment period, tumor sizes and body weights of mice were recorded every other day. As displayed in Figs. 4C and D, the tumor volumes in the PBS + L and Ru2@BSA + D groups increased by about 20 times after 16 days. In sharp contrast, Ru2@BSA + L could significantly inhibit tumor growth, indicating its efficient phototherapeutic efficacy *in vivo*. In addition, the mean tumor weight of Ru2@BSA + L group was only about 14% of that of other two groups (Fig. 4E). No significant change in body weight was observed throughout the entire treatment period, indicating the good biocompatibility of Ru2@BSA (Fig. 4F). After 16 days, the tumor tissues and main organs (including heart, liver, spleen, lung, and kidney) of mice were collected for staining analysis. Hematoxylin and eosin (H&E) and terminal deoxynucleotidyl transferase dUTP nick end labeling (TUNEL) staining results displayed that only Ru2@BSA + L could cause significant damage to the tumor tissues (Fig. 4G). No obvious tissue damage/abnormality was observed for the main organs (Fig. S35 in Supporting information), consistent with the good biocompatibility of Ru2@BSA.

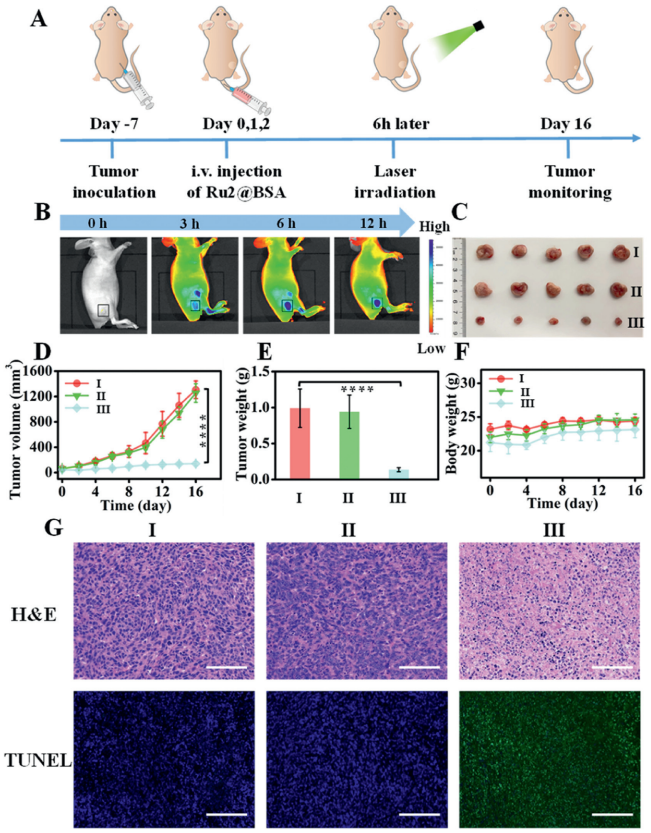

Fig. 4. (A) Timeline for *in vivo* experiments. (B) *In vivo* fluorescence images of a tumor-bearing mouse after intravenous injection of Cy5.5-labeled Ru2@BSA. The tumor is marked by a black box. (C) Photos of the tumors harvested at day 16 after different treatments. (D) Tumor volume measurement for different groups. (E) Mean tumor weights after different treatments. (F) Body weight changes of the mice under different treatments. (G) H&E and TUNEL staining of the tumor tissues. Scale bar: 100 μm. Data were presented as mean ± SD ($n = 5$). $^{****}P < 0.0001$, two-tailed Student's *t*-test.

In summary, two novel Ru(II) AIE agents with efficient PDT activity were reported in this work. Ru1 and Ru2 possess long ^{3}MLCT lifetimes (about 1 μs) and high singlet oxygen quantum yields (0.90 for Ru1 and 0.97 for Ru2) in H_2O. Noteworthy, Ru1 and Ru2 also exhibited potent photo-catalytic NADH oxidation with TOF values of about 1779 and 2000 h^{-1}, which are much higher than those of previously reported Ru(II) complexes under the same conditions. Ru1 and Ru2 could efficiently produce ROS and deplete NADH within cancer cells, therefore displaying good PDT activity *in vitro*. To enhance the tumor targeting ability *in vivo*, Ru2 was further loaded in BSA, and the resultant Ru2@BSA nanoparticles could selectively accumulate in tumor tissues and effectively inhibit tumor growth upon light irradiation. To the best of our knowledge, this is the first report of Ru(II) AIE agents with both high singlet oxygen quantum yield and potent photo-catalytic NADH oxidation activity. These findings can provide new insights for the development of efficient PDT agents with multiple anticancer mechanisms.

Declaration of competing interest

The authors declare that they have no known competing financial interests or personal relationships that could have appeared to influence the work reported in this paper.

CRediT authorship contribution statement

Yunli Xu: Data curation, Investigation, Visualization, Writing – original draft. **Xuwen Da:** Methodology, Investigation. **Lei Wang:** Methodology, Investigation. **Yatong Peng:** Validation, Formal analysis. **Wanpeng Zhou:** Validation, Formal analysis. **Xiulian Liu:** Project administration. **Yao Wu:** Project administration. **Wentao Wang:** Formal analysis. **Xuesong Wang:** Resources, Conceptualization, Supervision, Funding acquisition, Writing – review & editing. **Qianxiong Zhou:** Resources, Conceptualization, Supervision, Funding acquisition, Writing – review & editing.

Acknowledgment

This work was financially supported by National Natural Science Foundation of China (NSFC, No. 22371289).

Supplementary materials

Supplementary material associated with this article can be found, in the online version, at doi:10.1016/j.cclet.2024.110168.

References

[1] F. Bray, M. Laversanne, H. Sung, et al., CA Cancer J. Clin. 74 (2024) 229–263.
[2] S.N. Bhatia, X. Chen, M.A. Dobrovolskaia, T. Lammers, et al., Nat. Rev. Cancer 22 (2022) 550–556.
[3] Q. Dai, L. Wang, E. Ren, et al., Angew. Chem. Int. Ed. 61 (2022) e2022116.
[4] L. Wang, L. Lankhorst, R. Bernards, Nat. Rev. Cancer 22 (2022) 340–355.
[5] M. Kolarikova, B. Hosikova, H. Dilenko, et al., Med. Res. Rev. 43 (2023) 717–774.
[6] L. Liu, H. He, Z. Luo, et al., Adv. Funct. Mater. 30 (2020) 1910176.
[7] X. Zhao, J. Liu, J. Fan, H. Chao, X. Peng, Chem. Soc. Rev. 50 (2021) 4185–4219.
[8] M. Li, Y. Shao, J.H. Kim, et al., J. Am. Chem. Soc. 142 (2020) 5380–5388.
[9] B. Yang, Y. Chen, J. Shi, Chem. Rev. 119 (2019) 4881–4985.
[10] Z. Zhou, J. Song, L. Nie, X. Chen, Chem. Soc. Rev. 45 (2016) 6597–6626.
[11] G.B. Bodedla, X. Zhu, W.Y. Wong, Aggregate 4 (2023) e330.
[12] L. Conti, E. Macedi, C. Giorgi, B. Valtancoli, V. Fusi, Coord. Chem. Rev. 469 (2022) 214656.
[13] C. Mari, V. Pierroz, S. Ferrari, G. Gasser, Chem. Sci. 6 (2015) 2660–2686.
[14] H. Huang, B. Yu, P. Zhang, et al., Angew. Chem. 127 (2015) 14255–14258.
[15] S. Monro, K.L. Colón, H. Yin, et al., Chem. Rev. 119 (2019) 797–828.
[16] J. Liu, A.W. Prentice, G.J. Clarkson, et al., Adv. Mater. 35 (2023) 2210363.
[17] Y. Yang, X. Zou, Y. Sun, et al., Inorg. Chem. 62 (2023) 9649–9660.
[18] D.V. Titov, V. Cracan, R.P. Goodman, et al., Science 352 (2016) 231–235.
[19] C. Cantó, Keir J. Menzies, J. Auwerx, Cell Metab. 22 (2015) 31–53.
[20] H. Huang, S. Banerjee, K. Qiu, et al., Nat. Chem. 11 (2019) 1041–1048.
[21] M. Li, K.H. Gebremedhin, D. Ma, et al., J. Am. Chem. Soc. 144 (2022) 163–173.
[22] K.X. Teng, L.Y. Niu, N. Xie, Q.Z. Yang, Nat. Commun. 13 (2022) 6179.
[23] X. Da, X. Liu, C. Li, et al., Chin. Chem. Lett. 34 (2023) 108317.
[24] X. Da, Z. Wang, Y. Jian, et al., Inorg. Chem. Front. 9 (2022) 2544–2556.
[25] S. Qi, Z. Jin, Y. Jian, et al., Chem. Commun. 57 (2021) 4162–4165.
[26] C. Zhang, X. Guo, X. Da, et al., Dalton Trans. 50 (2021) 10845–10852.
[27] C. Zhang, J. Huang, X. Guo, et al., Nano Today 50 (2023) 101824.
[28] M. Li, Y. Xu, Z. Pu, et al., Proc. Natl. Acad. Sci. U. S. A. 119 (2022) e2210504119.
[29] J. Luo, Z. Xie, J.W.Y. Lam, et al., Chem. Commun. (2001) 1740–1741.
[30] M. Kang, Z. Zhang, N. Song, et al., Aggregate 1 (2020) 80–106.
[31] M. Li, Y. Gao, Y. Yuan, et al., ACS Nano 11 (2017) 3922–3932.
[32] Z. Zhang, M. Kang, H. Tan, et al., Chem. Soc. Rev. 51 (2022) 1983–2030.
[33] Z. Zhao, H. Zhang, J.W.Y. Lam, B.Z. Tang, Angew. Chem. Int. Ed. 59 (2020) 9888–9907.
[34] L. Fang, Q. Meng, Y. Zhang, et al., ACS Nano 17 (2023) 21553–21566.
[35] P. Xiao, W. Xie, J. Zhang, et al., J. Am. Chem. Soc. 145 (2023) 334–344.
[36] J. Zhuang, B. Wang, H. Chen, et al., ACS Nano 17 (2023) 9110–9125.
[37] A.O. Elzoghby, W.M. Samy, N.A. Elgindy, J. Control. Rel. 157 (2012) 168–182.
[38] F. Jiang, B. Ding, S. Liang, et al., Biomaterials 268 (2021) 120545.
[39] Z. Liu, X. Chen, Chem. Soc. Rev. 45 (2016) 1432–1456.
[40] S. Wang, Y. Pang, S. Hu, et al., Chem. Eng. J. 451 (2023) 138864.
[41] C. Tanielian, C. Wolff, M. Esch, J. Phys. Chem. 100 (1996) 6555–6560.
[42] Z. Fan, J. Xie, R. Kushwaha, et al., Chem. Asian J. 18 (2023) e202300047.
[43] A.K. Mengele, D. Weixler, A. Chettri, et al., Chem. Eur. J. 27 (2021) 16840–16845.
[44] S. Zhang, J. Shi, Y. Chen, et al., ACS Catal. 10 (2020) 4967–4972.
[45] W. Li, S. Yin, Y. Shen, et al., J. Am. Chem. Soc. 145 (2023) 3736–3747.
[46] L. Wei, X. He, D. Zhao, et al., Eur. J. Med. Chem. 264 (2024) 115985.
[47] A. Chiarugi, C. Dölle, R. Felici, M. Ziegler, Nat. Rev. Cancer 12 (2012) 741–752.
[48] S. Paglin, N.Y. Lee, C. Nakar, et al., Cancer Res. 65 (2005) 11061–11070.
[49] N. Tian, W. Sun, X. Guo, et al., Chem. Commun. 55 (2019) 2676–2679.
[50] H. Maeda, J. Wu, T. Sawa, Y. Matsumura, K. Hori, J. Control. Rel. 65 (2000) 271–284.